Biosensors and Bioelectronics 185 (2021) 113269

Contents lists available at ScienceDirect

Biosensors and Bioelectronics

journal homepage: http://www.elsevier.com/locate/bios

Specific intracellular binding peptide as sPD-L1 antibody mimic: Robust binding capacity and intracellular region specific modulation upon applied to sensing research

Junjie Hu [a], Zhao-huan Zhang [b], Zhongzheng Zhu [c], Jie Chen [a,d], Xiaojun Hu [a], Hongxia Chen [a,*]

[a] Center for Molecular Recognition and Biosensing, School of Life Sciences, Shanghai University, Shanghai, 200444, PR China
[b] Department of Laboratory Medicine, Changzheng Hospital, Naval Medical University, Shanghai, 200003, PR China
[c] Department of Oncology, Shanghai Tenth People's Hospital, Tongji University School of Medicine, 301 Middle Yanchang Road, Shanghai, 200072, PR China
[d] School of Medicine, Shanghai University, Shanghai, 200444, PR China

ARTICLE INFO

Keywords:
Programmed death ligand 1
Surface plasmon resonance
Specific intracellular binding peptide
Gold nanoparticles
Serum sample

ABSTRACT

Programmed death ligand 1 (PD-L1) immune checkpoint has been regarded as a new target for predicting cancer immunotherapy. As a transmembrane protein, PD-L1 has very low blood concentration and is likely to deplete their native activity when separated from the membrane environment due to significant hydrophobic domains, which make it difficult to measure sensitively. The reported PD-L1 aptamers and antibodies are both extracellular region binding molecules with the overlapping binding sites, which seriously limit with the construction of biosensor. Specific intracellular binding peptide (SIBP) as a unique PD-L1 intracellular region homing probe molecule is utilized for specifically capture targets. A simple and sensitive surface plasmon resonance (SPR) sandwich assay was constructed to detect serum soluble PD-L1 (sPD-L1) based on the unique and strong binding ability of SIBP to the intracellular region of sPD-L1. The designed SPR sensor showed great selectivity and wide dynamic response range of sPD-L1 concentration from 10 ng/mL to 2000 ng/mL. The limit of detection was calculated to be 1.749 ng/mL (S/N = 3). Owing to the SIBP's strong and specific binding ability with sPD-L1, the sensitive sensor can successfully detect sPD-L1 in serum samples, paving the way for the development of efficient test tools for clinical diagnosis and analysis.

1. Introduction

Cancer is one of the top leading causes of mortality and a major public disease worldwide (Bray et al., 2018). To date, common cancer treatments include surgical resection, radiotherapy and chemotherapy, which exhibit limited curative effects for patients, especially for advanced cancer (Chen et al., 2013; Zou et al., 2016). A large number of recent studies showed that immune-checkpoint blockade therapies against programmed cell death receptor 1 (PD-1) and programmed death ligand 1 (PD-L1) have been the focus of cancer research due to their substantial clinical benefits in different cancers (Brownlie et al., 2019; Lyu et al., 2019). PD-L1 has become a crucial biomarker for predicting efficacy of anti-PD-1/PD-L1 monoclonal antibody (mAb) and has been approved by the U.S. Food and Drug Administration (FDA) as companion diagnosis (CD) for immunotherapy. The PD-L1 clinical test can help precision medicine for maximized treatment outcome, thereby reducing the waste of medical resources and unnecessary patient expenditures (Collins and Varmus 2015; Davis and Patel 2019).

Peptides have attracted great interest in many fields due to their small size and large-scale chemical synthesis. The specific intracellular binding between peptides and their target proteins is derived from the evolution of natural peptide and exhibit few off-target effects in in vivo tests, which gives peptides enormous potential to exploit related targeted drugs (Araste et al., 2018; Jiang et al., 2019). In addition, peptides own slighter drug-drug interaction and less immunogenic than mAbs or proteins, and will not accumulate in the kidney, liver, or any other organs (Lu et al., 2017; Wei et al., 2018). Therefore, the design of new peptide-based drugs can achieve better treatment outcome and lower clinical immunogenicity. The simple chemical structure of small peptides makes them easy to be modified, while biological macromolecule antibodies can hardly be arbitrarily modified without impairing their affinities (Jung et al., 2019; Zhai et al., 2020; Wei et al., 2015; Akter

* Corresponding author.
E-mail address: hxchen@shu.edu.cn (H. Chen).

https://doi.org/10.1016/j.bios.2021.113269
Received 13 January 2021; Received in revised form 30 March 2021; Accepted 16 April 2021
Available online 23 April 2021

et al., 2012). Furthermore, peptides can be flexibly immobilized on the different nanomaterials, such as metal nanoparticles or liposomes, which make them have promising potential in the development of sensing (Liu et al., 2018; Qi et al., 2018).

Huntington interacting protein 1 related protein (HIP1R) can specifically bind with the intracellular region of PD-L1 and affect PD-L1 lysosome degradation, thereby regulating T cell-mediated tumor killing (Scheme 1A) (Wang et al., 2019a,b). The sequence of H-DKEMAATSAAIEDAVRRIEDMMNQMDFSGC-OH in HIP1R was found to bind PD-L1 as a specific intracellular binding peptide (SIBP). The designed SIBP showed strong binding force compared with that of antibodies. Combing the peptide's merits and strong binding ability with PD-L1, SIBP may pave the way for further sensing and drug discovery application.

Increasing evidence indicated that the level of soluble PD-L1 (sPD-L1) in peripheral blood was associated with the clinicopathological characteristics, treatment response, and prognosis of patient in various tumor types (Hejleh et al., 2019). However, its sensitive detection is limited due to its low concentration in serum and various body fluids. Currently, several enzyme-linked immunosorbent assay (ELISA) systems for the detection of plasma sPD-L1 have been reported (Chen et al., 2011; Takeuchi et al., 2018). Nevertheless, there are certain limitations with ELISA systems, such as time-consuming incubation, low reproducibility and low sensitivity, which may hinder their widespread applications. In addition, polymerase chain reaction (PCR) has been used to detect PD-L1 mRNA, taking PD-L1 mRNA as a template for amplification detection, and analysed pathological conditions based on mRNA levels. Since most of the correlations between PD-L1 mRNA and protein levels in many cancers are not statistically significant (Goltz et al., 2016; Xue et al., 2018), PCR cannot show the pathological state of the disease exactly. Therefore, it is urgent to develop a fast, accurate and sensitive biosensor for sPD-L1 detection.

Antibodies and aptamers are often used as specific probes to identify and detect targets in biosensors (Huang et al., 2020c; Pang et al., 2020). Currently, the reported PD-L1 aptamers and antibodies are both extracellular region binding molecules with the overlapping binding sites, which seriously limit the construction of biosensor (Yang and Hu 2019). In addition, compared with antibodies, some aptamers obtained from screening phage display libraries have weaker binding affinity and selectivity, which limit the performance of biosensors. As a specific capture molecule in the intracellular region of sPD-L1, SIBP is an alternative choice which can eliminate the interference of steric hindrance when fabricating a sandwich sensing platform, which can achieve specific and sensitive detection through simple signal amplification.

In this work, we designed a facile and sensitive surface plasmon resonance (SPR) sensor to detect sPD-L1 (Scheme 1B). sPD-L1 can be immobilized on the Au film in a facile manner through binding to Anti-PD-L1. The SIBP-functionalized AuNPs specifically interact with sPD-L1, which contributes to the significant change in SPR signal and improves detecting selectivity. A highly sensitive and selective format for sPD-L1 measurement is fabricated to provide a possible solution for the detection of clinical sPD-L1. It can be served as an important template for the development and application of SIBP and other natural peptides in various fields.

2. Experimental section

2.1. Reagents and apparatuses

Gold (III) chloride hydrate ($HAuCl_4 \bullet 3H_2O$), sodium citrate tribasic dehydrate, potassium phosphate monobasic (KH_2PO_4), 1-ethyl-3-(3-dimethylaminopropyl) carbodiimide hydrochloride (EDC), N-hydroxysulfosuccinimide (NHS), sodium chloride (NaCl) and potassium chloride (KCl) were purchased from Sigma-Aldrich, Inc. (St. Louis, USA). Disodium hydrogen phosphate (Na_2HPO_4) and bovine serum albumin (BSA) were purchased from Sinopharm Chemical Reagent Co., Ltd. (Shanghai, China). Anti-PD-L1 and programmed death ligand-1 (PD-L1) were bought from Abcam (Abcam, China, ab184919). *para*-Sulfonatocalix[4]arene (pSC_4) was produced from TCI Development Co., Ltd. (Shanghai, China). SIBP was synthesized by GL Biochemistry Ltd. (Shanghai, China). SIBP: H-DKEMAATSAAIEDAVRRIEDMMNQMDFSGC-OH. All chemical reagents were analytical grade. All solutions were treated with deionized water (DW) and purified by a Milli-Q distillation system (18.2 MΩ cm, Branstead, USA).

UV–vis spectrum was recorded on a Shimadzu UV-2450 PC UV–vis spectrophotometer (Shimadzu, Japan). Surface modification was monitored by Fourier transform infrared (FT-IR) spectroscopy (Bruker 70, Germany). Transmission electron microscopic (TEM) image was produced by a JEM-2010F microscope (Japan). Atomic force microscope (AFM) images were performed by Agilent 5500 (Santa Clara, USA). Samples were imaged in contact mode at ambient temperature. The ζ potential and dynamic light scattering (DLS) data were carried with a Malvin Zetasizer 3000HS system. Electrochemical measurements were conducted with an Autolab PGSTAT128N system (Eco Chemise B.V., The Netherlands). The SPR spectroscopic measurements were recorded with a multiparametric surface plasmon resonance device (MP-SPR Model Navi™ 210A, Oy BioNavis Ltd., Finland). The SPR chips bought from BioNavis were consisted of Schott glass D263 (thickness 0.5 mm)

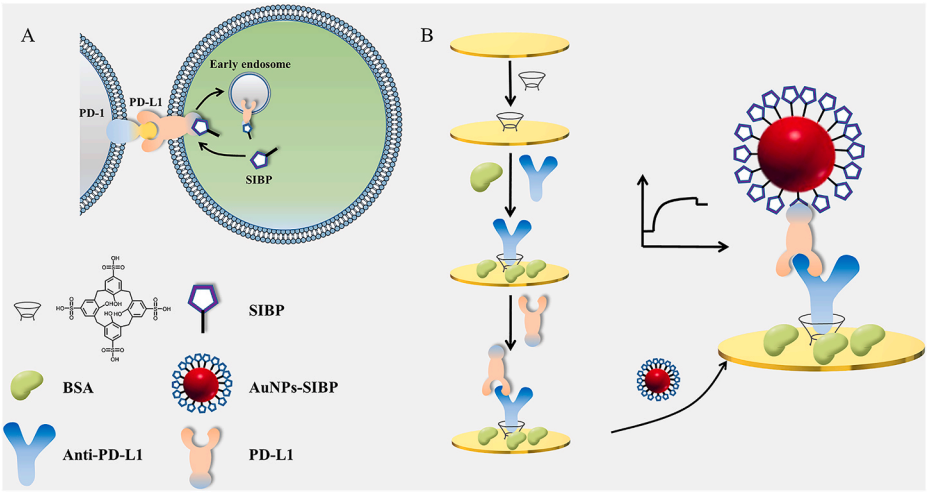

Scheme 1. A) A representation of SIBP mediates PD-L1 degradation in cancer cells, to mimic its characteristic to bind to the intracellular domain of PD-L1. B) Schematic of a simple natural peptide-based immune SPR sensor for detecting sPD-L1.

sputter-coated with Au and a Cr adhesive layer (total thickness 52 nm).

2.2. Synthesis of AuNPs and AuNPs-SIBP

AuNPs colloidal solution used in this work was synthesized by citrate reduction of $HAuCl_4 \bullet 3H_2O$ in a one-pot process. First of all, 1 mL of 0.1% $HAuCl_4$ solution was added to the vortex of the 95.5 mL of deionized water for boiling of 5 min. Subsequently, 3.5 mL of 1% sodium citrate solution was rapidly added into the round-bottom flask for 20 min. The color of the solution immediately changed from yellow to wine red, setting out the formation of AuNPs. The solution was naturally cooled to room temperature and stirring was continued for another 45 min. The as-prepared of AuNPs colloids was stored in an amber bottle at 4 °C.

According to the previous study, peptide modified AuNPs were prepared (Xiong et al., 2017) through forming Au–S bond between the thiol group (-SH) of the cysteine and the AuNPs. 200 μL of 100 μg/mL SIBP solution was prepared and reacted with 4800 μL AuNPs colloidal solution for overnight after completion shaking. After centrifugation at 10,000 g for 10 min, precipitation were re-dissolved into deionized water to remove unbound peptides. The prepared AuNPs and AuNPs-SIBP were characterized using UV–vis spectrum.

2.3. Stability of AuNPs-SIBP

The stability of the synthesized AuNPs-SIBP was studied. AuNPs-SIBP was stored in a refrigerator at 4 °C followed by DLS and Zeta potential measurements at predetermined time intervals of 120 h. Finally, the DLS and Zeta potential of AuNPs-SIBP were recorded within 15 days.

2.4. Binding kinetics experiment

100 μL of 10 mM pSC_4 was dropped and incubated on the surface of the SPR chip overnight, and then 300 μL of PD-L1 protein was injected on the SPR instrument at a flow rate of 5 μL/min. BSA was used to block the free sites at a flow rate of 10 μL/min after washed with deionized water. Anti-PD-L1 (0.012, 0.024, 0.047, 0.094, 0.118 and 1.18 μM) and SIBP (0.04, 0.1, 0.2, 0.4, 0.8, 1 and 10 μM) were respectively subjected to binding kinetic experiments. SPR signal changes were detected using a MP-SPR. For equilibrium dissociation constant determination, serial dilution method was used and the KD of SIBP for sPD-L1 protein was calculated with equation (1) (Lai et al., 2016).

$$Y = \frac{B_{max} * x}{K_D + x} \quad (1)$$

2.5. Fabrication of PD-L1 biosensor and detection

The desired gold chip was initially rinsed with ethanol and deionized water. Following this, the bare chip was soaked in piranha solution (98% H_2SO_4: 30% H_2O_2 = 3:1) for 40 s, then rinsed with DW and dried with nitrogen. Subsequently, 10 mM pSC_4 solution was incubated on the gold chip at room temperature overnight, and the surface was further rinsed with DW. The prepared gold chip was set on the SPR instrument.

After pSC_4 was immobilized on the chip, 300 μL of 2.35 μg/mL Anti-PD-L1 was flowed on the chip at a flow rate of 5 μL/min. The Anti-PD-L1 was capable of specifically binding with pSC_4 through host-guest recognition within 40 min. Then, the surface of gold chip was rinsed with buffer to remove the uncombined Anti-PD-L1. The surface was sealed with 0.1 mg/mL BSA to avoid non-specific adsorption. Different concentrations of sPD-L1 were flowed and reacted on the surface of the gold chip about 40 min for the detection process (10, 50, 100, 200, 300 and 2000 ng/mL). The residual sPD-L1 was removed by washing with buffer solution. Given the natural binding affinity of SIBP with the intracellular region of sPD-L1, the signal could be further amplified by 300 μL of AuNPs-SIBP (100 μg/mL). Finally, the SPR response was monitored until a stable baseline was received. In order to study the sensor's selectivity, 2 μg/mL Siglec-15, Ascorbic acid (AA), Glucose, Dopamine (DA), and Histidine (His) were added onto the gold chip. The SPR signal changes were compared with that of 200 ng/mL sPD-L1.

2.6. Preparation of the modified electrodes and the measurement produce

The gold electrode (GE) (3.0 mm diameter) was firstly cleaned with deionized water. After that, the electrode was polished with 1, 0.3 and 0.05 μm alumina powder, respectively. Sequentially, the electrode was sonicated in deionized water, ethanol and deionized water (5 min, respectively). Then, the GE was cleaned with piranha solution (98% H_2SO_4:30% H_2O_2 = 3:1) for 30 s to remove the remaining impurities, and finally rinsed with deionized water. Afterward, the electrode was cleaned with an electrochemical method (cyclic voltammetry activation, 0–1.6 V, 20 cycles) with 0.5 M H_2SO_4. Finally, the electrode surface was purged and dried by nitrogen. The gradual modification of the electrode was consistent with the construction process of the SPR chip.

The cyclic voltammetry (CV) and electrochemical impedance spectroscopy (EIS) were performed on a model Autolab PGSTAT128 N system using a typical three-electrode cell at room temperature. EIS data was performed within the frequency range from 0.1 Hz to 100 kHz. CV measurement was carried in the potential from −0.8 V to 0.8 V at 50 mV/s scan rate. The CV and EIS characterizations were processed in 5 mM $[Fe(CN)_6]^{3-/4-}$ solution containing 0.1 M KCl.

2.7. sPD-L1 analysis in clinic patient samples

Human serum samples were collected from healthy donors and patients at different stages from Shanghai Tenth People's Hospital, Shanghai, China. All experiments on clinical samples were approved by the Medical Research Ethics Committee, Shanghai Tenth People's Hospital, Shanghai, China. The serum samples were collected from each blood donors and centrifuged at 1500 rpm for 20 min to remove the precipitate. The supernatant was further centrifuged at 1200 rpm for 20 min to obtain the supernatant of the centrifuged product, and preserved at −20 °C prior to use. After diluted to 1:100, 400 μL of the sample was flowed on the surface of gold chip to perform clinical samples analysis.

3. Results and discussion

3.1. Characterization of AuNPs-SIBP

UV–vis spectroscopy, dynamic light scattering, Zeta potential, and Fourier transform infrared spectroscopy were used to confirm the successful synthesis and modification of AuNPs-SIBP. A SPR band of AuNPs was observed at 518 nm and TEM image of AuNPs with a size of 10 ± 2 nm (Fig. 1 (A) insert) confirmed the uniformly dispersed spherical structure of the synthesized particles, as shown in Fig. 1 (A). The large specific surface area of AuNPs can achieve surface chemical modification easily through Au–S bond and give specific functions (Jiang et al., 2017). Moreover, the assembly of AuNPs and SIBP was studied by UV–vis spectroscopy. No specific absorption peak was observed for SIBP only. After modification, the resonance absorption peak of AuNPs-SIBP appeared at 527 nm, the formation of Au–S bond made the maximum plasmonic absorption peak slight red-shift comparing with that of AuNPs, indicating that SIBP was successfully linked with AuNPs. The decreased absorbance may be attributed to the addition of SIBP and several times of centrifugations and re-dissolving during the synthesis of AuNPs-SIBP.

In order to evaluate the coupling of AuNPs and SIBP, FT-IR spectroscopy was utilized to analyze the infrared spectra corresponding to AuNPs and AuNPs-SIBP. According to the spectrum in Fig. 1 (C), specific functional groups of the active ingredients were identified based on the peak positions. The strong stretching vibration of C═O of the amide bond located at 1642 cm^{-1} and the in-plane deformation vibration of

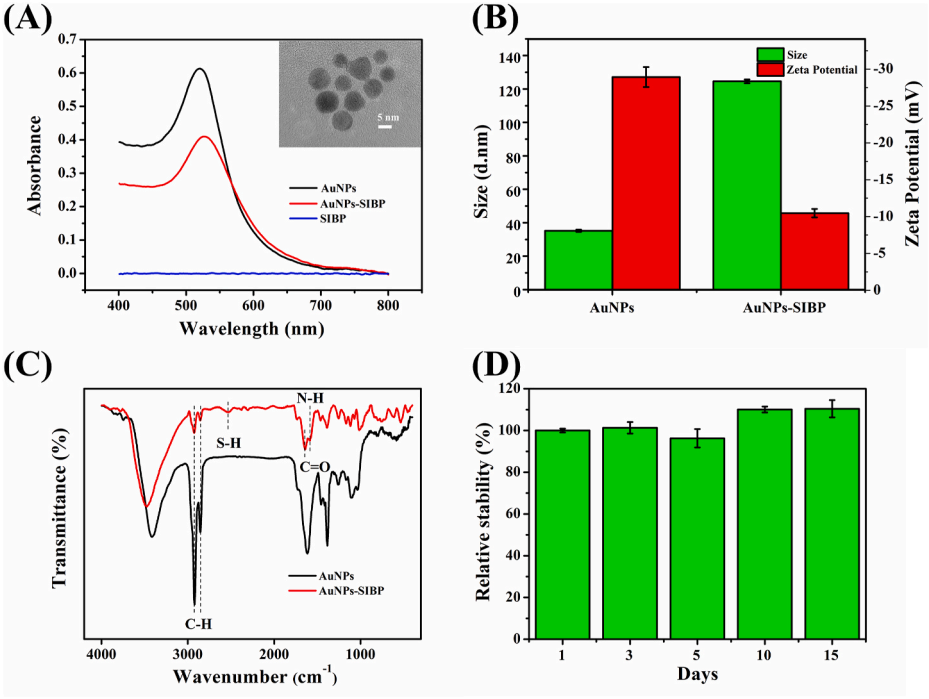

Fig. 1. A) UV–vis spectra of SIBP (blue), AuNPs before (black) and after (red) SIBP modification. The inset is the TEM image of AuNPs. B) DLS (green) and Zeta potential (red) data of before and after modification of AuNPs. C) FT-IR spectroscopy of AuNPs and AuNPs-SIBP. D) Stability of AuNPs-SIBP at different time conditions. Error bars indicate standard deviations of tests (n = 3). (For interpretation of the references to color in this figure legend, the reader is referred to the Web version of this article.)

NH_2 at 1587 cm^{-1} were more intense, indicating the introduction of peptide bonds (Ma et al., 2012). In addition, the SH stretching peak at 2527 cm^{-1} also confirmed that SIBP was successfully modified on the surface of AuNPs (Bare et al., 1975).

The changes in hydrodynamic diameter and surface charge of nanoparticles before and after SIBP functionalization were shown in Fig. 1 (B). DLS showed that the mean equivalent hydrodynamic diameters of AuNPs and AuNPs-SIBP were 35.15 ± 0.68 nm and 124.60 ± 1.14 nm respectively. The zeta potential decreased from −28.93 ± 1.36 mV of AuNPs to −11.47 ± 0.57 mV of AuNPs-SIBP. The hydrodynamic radius of AuNPs based on DLS was larger than that observed directly by TEM, which is due to the subtle difference in hydration status and the intensity-based weighting of the DLS data (Lim et al., 2013). The zwitterionic peptide SIBP replaced the strong anionic sodium citrate on the surface of AuNPs, resulting in a decrease of the charges on the particle surface (Thielbeer et al., 2011), thereby weakening the electrostatic repulsive force between individual nanoparticles, and increasing the hydrodynamic diameter of AuNPs-SIBP to 124.60 nm. These values are in good agreement with the previously reported for 25-amino acid-long peptides grafted onto AuNPs (Duy et al., 2010). Therefore, these results support the successful formation of AuNPs-SIBP.

To observe the stability of AuNPs-SIBP, the hydrodynamic diameter of AuNPs-SIBP was measured and then compared with the initial data as shown in Fig. 1 (D). Diameter of AuNPs-SIBP changed only 10.41% after 15 days' storage at 4 °C, indicating that the synthesized material has good stability (Huang et al. 2020a, 2020c). In summary, the construction of AuNPs-SIBP was successfully proved. The prepared AuNPs-SIBPs were used in subsequent experiments.

3.2. Comparison experiment of binding force and the feasibility of biosensors

The binding affinity of SIBP and Anti-PD-L1 to sPD-L1 was evaluated by SPR (Wu et al., 2020). It is well known the strong binding is very important for construction of sensitive sandwich assay. As shown in Fig. 2 (A), SPR results showed that the dissociation constant (KD) of Anti-PD-L1 to the extracellular domain of sPD-L1 was 217.36 nmoL/L, which was consistent with the value tested by ELISA (Huang et al., 2020b). The 30-amino acid-long SIBP specifically bound to the intracellular region of sPD-L1 with KD of 883.77 nmoL/L. The interactions between SIBP/Anti-PD-L1 and sPD-L1 are strong enough so that both can attain comparable amplitudes. The SPR real time spectroscopy for adding different concentrations of Anti-PD-L1 or SIBP was shown in Fig. S1 and S2. The strong binding affinity and better stability makes SIBP have greater application prospects. In addition, natural SIBP as a mimic antibody can be obtained without tedious selecting process like aptamers. Also, most of the PD-L1 aptamers or antibodies are both extracellular domain binding molecules, which limit to fabricate efficient sandwich structures due to steric hindrance. Therefore, SIBP is of great significance to be used as a sandwich structure recognition component.

A SPR sensing platform based on AuNPs-SIBP was designed to realize the selective detection of trace and important serum sPD-L1. SPR was used to monitor the modification of each step in real time and verify the response process of the constructed sensor. Gold atoms on the surface of the SPR chip covalently bound with the $–SO_3$ of *para*-Sulfonatocalix[4]arene (pSC_4) to form an Au–S bond, which fixed on the gold chip. Previous study confirmed that pSC_4 can be effectively linked to $–NH_2$ on the Anti-PD-L1 by host-guest recognition (Mei et al., 2012). In addition, calixarene is used as a commonly protein linker because it maintains natural activity of antibodies through several soft non-covalent bonds.

The SPR angle increased 195 m° when Anti-PD-L1 flowed through the gold chip at a certain flow rate, as shown in Fig. 2 (B). This result verified the feasibility of interacting between Anti-PD-L1 and pSC_4 (Zhou et al., 2017). BSA was added as the blocking molecule to prevent nonspecific binding on the gold chip and resulted in 77 m° SPR angle shift. The addition of a trace amount of sPD-L1 protein caused slight SPR angle changes. The specific recognition between the extracellular region of sPD-L1 and Anti-PD-L1 would expose the intracellular region to bind SIBP modified AuNPs specifically, resulted in a significant change in the SPR angle (93 m°). As shown in Fig. 2 (C), the SPR signal changes caused by SIBP only and AuNPs-SIBP-sPD-L1 were nearly 3 times and 6 times than that of direct sPD-L1 detection, respectively. Therefore, the above results showed that this method has good SPR feasibility, and AuNPs-SIBP can be the effective means for sPD-L1 sensor signal amplification.

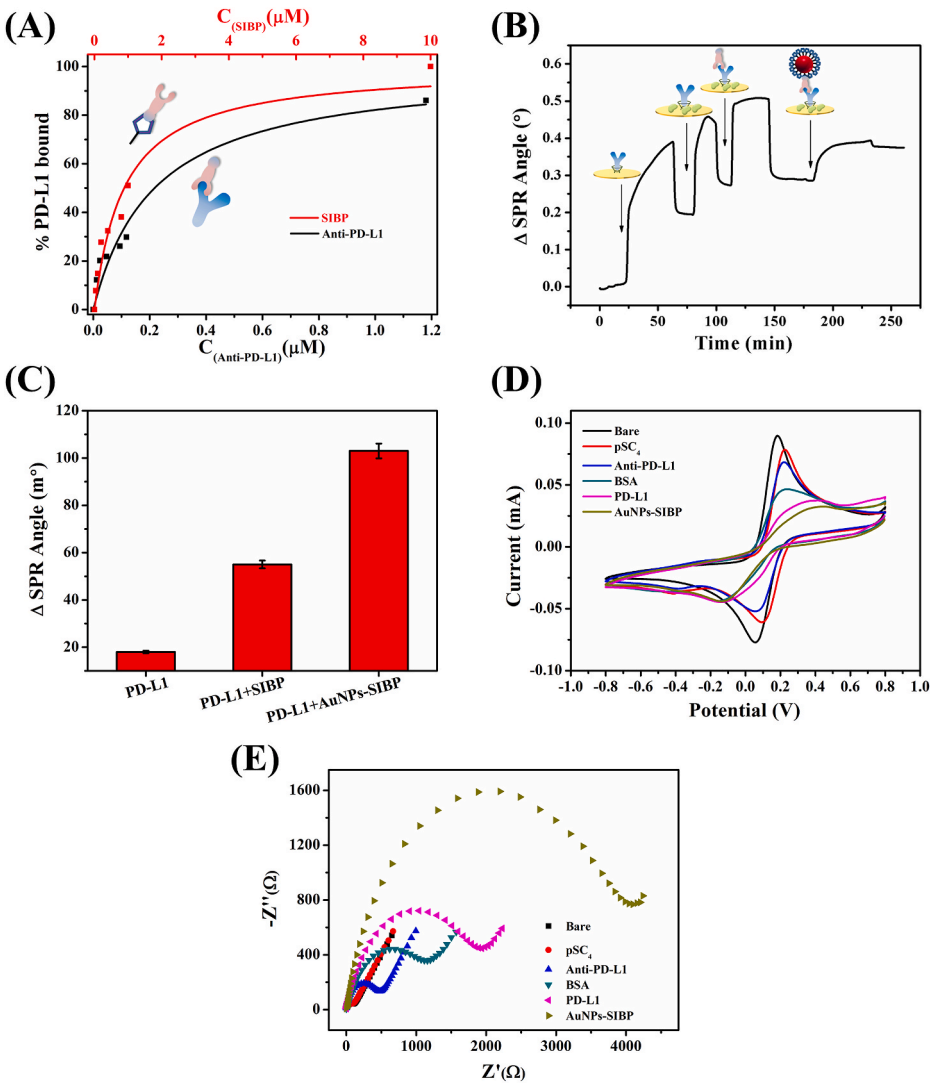

Fig. 2. A) The equilibrium dissociation constant of SIBP (red) and Anti-PD-L1 (black) to sPD-L1 was determined using a SPR gold chip binding experiment. B) Real-time SPR sensorgram of step-by-step manufacturing process. C) Different SPR angle shift after the addition of protein, protein-SIBP and protein-AuNPs-SIBP under the same sPD-L1 protein concentration. CV D) curves and EIS E) Nyquist plots of stepwise modification at gold electrode. (For interpretation of the references to color in this figure legend, the reader is referred to the Web version of this article.)

CV and EIS are usually used to study gradual modification process and molecular assembly on the electrode surface (Zhu et al., 2020). Bare GE presented extremely small impedance and high redox peak current, which was attributed to its strong electron transfer ability (Fig. 2 (D) and (E)). The electron transfer of $[Fe(CN)_6]^{3-/4-}$ would be hindered since pSC_4 was negatively charged, thereby resulting in an increase in R_{ct} value and a decrease in CV peak. The step-by-step modification with Anti-PD-L1, BSA, and sPD-L1 all showed increased R_{ct} values and reduced peak current, owing to the high charge transfer resistance of proteins. The SIBP-PD-L1 protein complexes formed by immune molecule-antigen interaction would cause an evidently increase in steric hindrance, which severely blocked the $[Fe(CN)_6]^{3-/4-}$ electron transfer (Tang et al., 2007). Therefore, after modified with AuNPs-SIBP, the R_{ct} value increased while the CV peak decreased correspondingly. The above results demonstrated the successful construction of the designed sPD-L1 sensor.

3.3. AFM morphology of the AuNPs-SIBP-based biosensor

Because of the ability of Atomic Force Microscope (AFM) to characterize the particle size distribution in the nanometer range, it is often utilized as an ideal tool to verify the effectiveness of sensor design (Zhao et al., 2019). 2D image and typical cross-sectional view in Fig. 3 showed the morphological changes of the sensor during the gradual modification process. Fig. 3 (A) demonstrated the bare gold chip exhibited excellent uniformity with a smaller surface roughness of about 3 nm. As shown in Fig. 3 (B), after the incorporation of sPD-L1, the surface roughness increased to 8 nm, which successfully exhibited the change in interface roughness. After AuNPs-SIBP were further modified to the chip surface through specific interaction between the intracellular region of sPD-L1 and SIBP, the surface roughness increased about 9 nm (Fig. 3 (C)), which corresponded to the size of AuNPs. Hence, these AFM image results supported the feasibility of the designed sensor.

3.4. Optimization of detection conditions

Experimental conditions of the sensor were optimized to achieve its maximum detection sensitivity. The Anti-PD-L1 concentration on the surface directly determined the amount of captured sPD-L1 antigen, so the Anti-PD-L1 concentration was optimized. As shown in Fig. 4 (A), the SPR angle shifts gradually increased as Anti-PD-L1 concentration increased and was almost saturated at 4.7 μg/mL, which may be related to the increased surface coverage of Anti-PD-L1 on the gold chip. The inset in Fig. 4 (A) indicated the corresponding step-by-step modification process. SPR angle shifts caused by 2.35 μg/mL was more than 88% of 4.7 μg/mL. In order to cut the cost of a single test, 2.35 μg/mL was selected as the Anti-PD-L1 concentration for subsequent experiments. The concentration of AuNPs-SIBP was the key factor of the sensor. According to the results shown in Fig. 4 (B), the SPR angle shifts increased along with the concentration of AuNPs-SIBP increasing, which showed

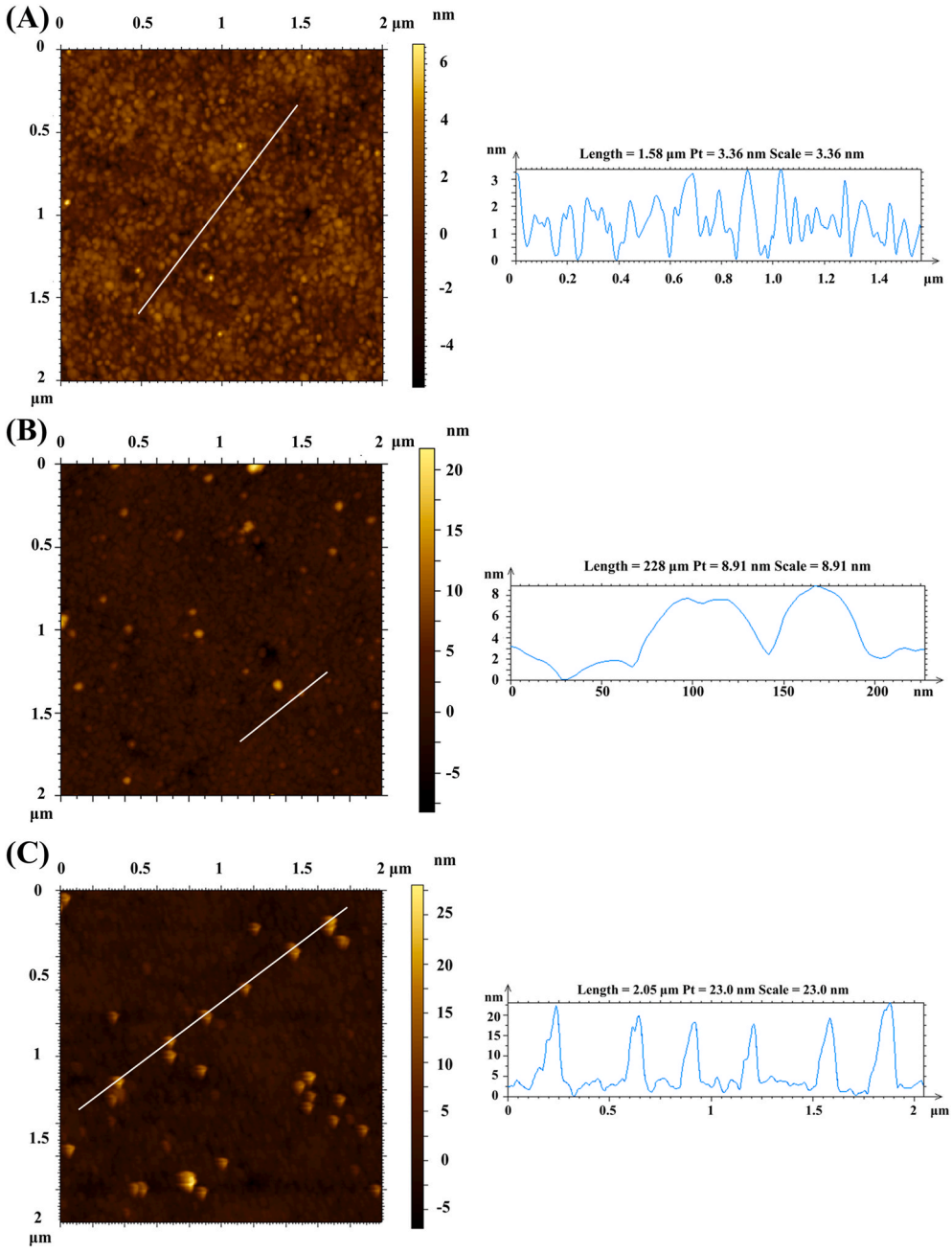

Fig. 3. AFM 2D images (left) and line profiles (right) of bare gold film A), protein modified surface B), and the sandwich structure modified surface C). (For interpretation of the references to color in this figure legend, the reader is referred to the Web version of this article.)

more AuNPs-SIBP were bound to the sensor through the specific interaction between SIBP and the intracellular region of sPD-L1, further achieved specific signal amplification for sPD-L1 detection. The inset demonstrated the modification process of AuNPs-SIBP at different concentrations. Since AuNPs-SIBP was almost saturated at 75 μg/mL, 75 μg/mL was choose as the best detection condition.

3.5. SPR performance and selectivity of PD-L1 sensor

In order to effectively improve sensitivity, the designed sensor was utilized to detect different concentrations of sPD-L1 under optimal conditions. Since the concentration of sPD-L1 in various cancer types or at different stages varies greatly (1.92–25 ng/mL), a wide detection range is required (Wang et al., 2015; Han et al., 2021; Zhu and Lang 2017). Different concentrations of sPD-L1 protein in the range of 10 ng/mL to 2000 ng/mL were added to immunologically interact with the Anti-PD-L1 molecules on the sensor interface. It can be seen from Fig. 4 (C) that the SPR angle shifts increased with the increased sPD-L1 captured amount and obtained a good linear relationship between the logarithm of sPD-L1 concentration and the SPR angle shift (Fig. 4 (D)). The linear regression equation was $Y = 35.104 + 25.855 \times \lg CPD\text{-}L1$, with the correlation coefficient $R^2 = 0.963$, and the limit of detection (LOD) calculated according to the rules of 3's blank criterion was 1.749 ng/mL. The LOD of this work was similar to the existing ELISA kits or sensors in Table S1, which was lower than the optimal prognosis value of sPD-L1 (1.92 ng/mL) in a variety of cancers according to previous reports (Xu et al., 2020). The sensor designed in this work owned a wider linear range and shorter detection time, which can better meet the demand of clinical detection of sPD-L1 and be used for patient prognosis, prediction of disease progression and treatment response.

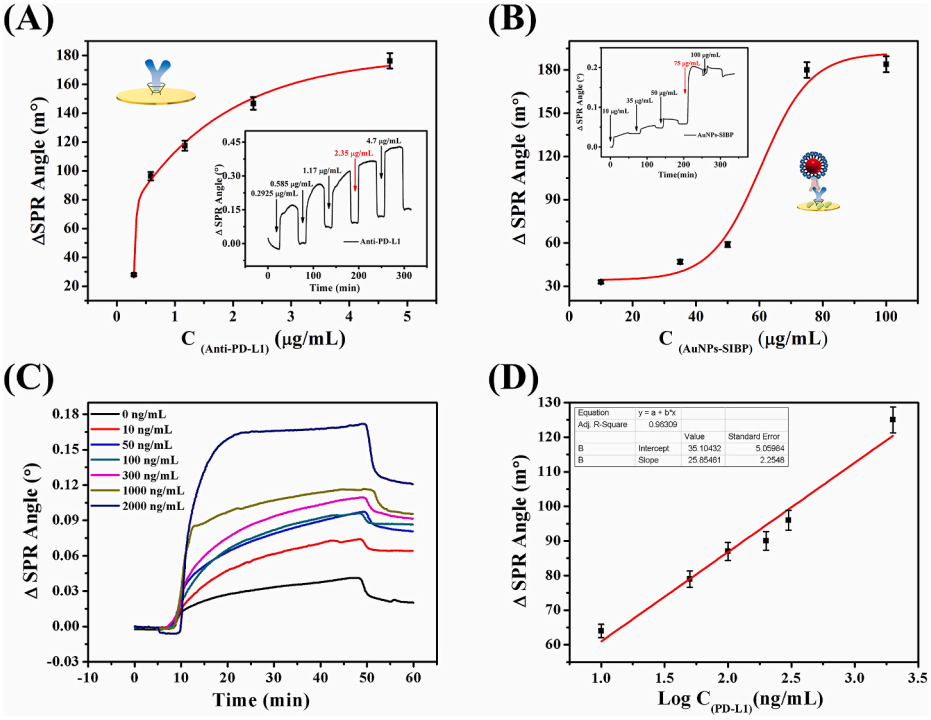

Fig. 4. A) Optimization of the antibody concentration. The inset shows the sensogram for AuNPs-SIBP sensors reacted with different concentrations of Anti-PD-L1 (0.292 μg/mL, 0.585 μg/mL, 1.17 μg/mL, 2.35 μg/mL, 4.7 μg/mL). B) Optimization of the AuNPs-SIBP concentration. The inset shows the sensogram for AuNPs-SIBP sensors reacted with different concentrations of AuNPs-SIBP (10 μg/mL, 35 μg/mL, 50 μg/mL, 75 μg/mL, 100 μg/mL). C) SPR angle shifts for the direct detection of PD-L1 at 10 ng/mL, 50 ng/mL, 100 ng/mL, 300 ng/mL, 1000 ng/mL, and 2000 ng/mL. D) Linear relationship for PD-L1 determination.

To verify the selectivity of the designed biosensor, a variety of interfering substances (2 μg/mL) were used for control experiments under the same conditions. Fig. S3 showed the original SPR spectra for different interfering substances and further amplified with AuNPs-SIBP. A variety of interferences (AA, Glucose, DA, His) that are widely presented in the serum did not cause significant SPR responses. Siglec-15 was the major immunosuppressive factor of PD-L1 negative tumors, which has the same function of suppressing immune response as PD-L1 (Wang et al., 2019a,b). Siglec-15 cannot give rise of large signal change, according to the immunological mechanism. As shown in Fig. 5 (A), the SPR angle change caused by PD-L1 was greater than that of other interfering substances, and showed a significant difference ($p < 0.0001$). The great selectivity for detection PD-L1 was achieved through dual specific binding among antibody, SIBP and sPD-L1.

3.6. sPD-L1 detection in clinical samples

The practicality of the assay was tested to detect the personal level of sPD-L1 in diluted serum from healthy donors and cancer patients. The SPR angle shifts of different clinical samples were compared as depicted in Fig. S4. As a consequence of the significant improvement of sensitivity of AuNPs-SIBP immunoassay, the SPR angle shifts caused by serum sPD-L1 concentrations of healthy donors and cancer patients were significant differences (*t*-test: $p < 0.005$), as shown in Fig. 5 (B). These results demonstrated the feasibility of the designed sensor to measure sPD-L1 in serum accurately and sensitively in future clinical testing, which assist the existing detection methods and reveal new mechanisms of immunotherapy.

4. Conclusion

In conclusion, a sensitive and simple sandwich assay was developed for sPD-L1 detection based on Anti-PD-L1, natural SIBP and sPD-L1. The unique and strong binding affinity of SIBP to the intracellular region of sPD-L1 broke the limitation of the traditional method in the detection of sPD-L1 due to the lack of immune molecules bound with the intracellular region. The steric hindrance was reduced and sensitive diagnosis of sPD-L1 at the ng/mL level with excellent specificity was realized in the detection. This strategy integrated the merits of natural biomolecules, host-guest recognition, and signal amplification of AuNPs, which could be applied to complex serum samples. This biosensor provides a tool for monitoring immune targets with great potential in the detection of

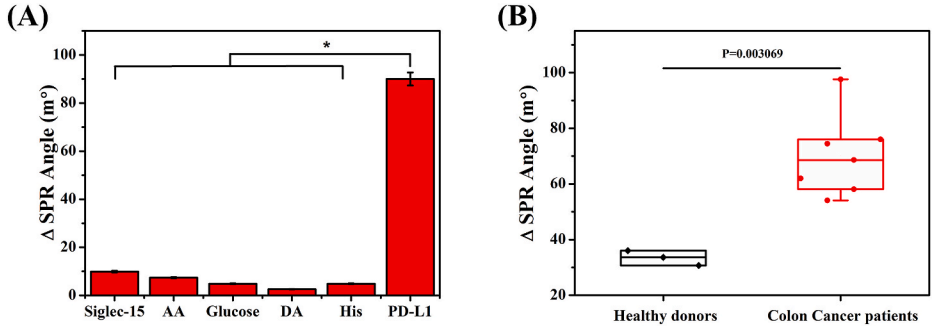

Fig. 5. A) SPR angle shifts of AuNPs-SIBP caused by different interfering substances; *$p < 0.0001$, compared with PD-L1. B) Comparison of the SPR angle shifts caused by serum sPD-L1 detected by AuNPs-SIBP sensor between healthy donors (n = 3) and colon cancer patients (n = 7). Statistical comparison of two groups was performed by *t*-test.

clinical biological samples, which can also be served as an important template for the development and application of SIBP in a variety of fields.

CRediT authorship contribution statement

Junjie Hu: Conceptualization, Data curation, Formal analysis, Validation, Writing – original draft. **Zhao-huan Zhang:** Formal analysis, Validation, Writing – original draft. **Zhongzheng Zhu:** Formal analysis, Writing – review & editing. **Jie Chen:** Data curation, Writing – review & editing. **Xiaojun Hu:** Funding acquisition, Writing – review & editing. **Hongxia Chen:** Conceptualization, Project administration, Funding acquisition, Writing – review & editing.

Declaration of competing interest

The authors declare that they have no known competing financial interests or personal relationships that could have appeared to influence the work reported in this paper.

Acknowledgements

This work was supported by the National Natural Science Foundation of China (Grant No. 61875114 and 62005156).

Appendix A. Supplementary data

Supplementary data to this article can be found online at https://doi.org/10.1016/j.bios.2021.113269.

References

Akter, F., Mie, M., Grimm, S., Nygren, P., Kobatake, E., 2012. Anal. Chem. 84, 5040–5046.
Araste, F., Abnous, K., Hashemi, M., Taghdisi, S.M., Ramezani, M., Alibolandi, M., 2018. J. Contr. Release 292, 141–162.
Bare, G.H., Alben, J.O., Bromberg, P.A., 1975. Biochemistry 14 (8), 1578–1583.
Bray, F., Ferlay, J., Soerjomataram, I., Siegel, R.L., Torre, L.A., Jemal, A., 2018. Ca - Cancer J. Clin. 68 (6), 394–424.
Brownlie, R.J., Wright, D., Zamoyska, R., Salmond, R.J., 2019. Jci Insight 4 (16), e127847.
Chen, E.Y., Dobrinski, K.P., Brown, K.H., Clagg, R., Edelman, E., Ignatius, M.S., Chen, J. Y.H., Brockmann, J., Nielsen, G.P., Ramaswamy, S., Keller, C., Lee, C., Langenau, D. M., 2013. PLoS Genet. 9 (8), e1003727.
Chen, Y., Wang, Q., Shi, B., Xu, P., Hu, Z., Bai, L., Zhang, X., 2011. Cytokine 56, 231–238.
Collins, F.S., Varmus, H., 2015. N. Engl. J. Med. 372, 793–795.
Davis, A.A., Patel, V.G., 2019. J. ImmunoTher. Cancer 7, 278.
Duy, J., Connell, L.B., Eck, W., Collins, S.D., Smith, R.L., 2010. J. Nanopart. Res. 12, 2363–2369.
Goltz, D., Gevensleben, H., Dietrich, J., Dietrich, D., 2016. OncoImmunology 6, e1257454.
Han, B., Dong, L., Zhou, J., Yang, Y., Guo, J., Xuan, Q., Gao, K., Xu, Z., Lei, W., Wang, J., Zhang, Q., 2021. Cancer Immunol. Immun, pp. 1–17.
Hejleh, T.A., Furqan, M., Ballas, Z., Clamon, G., 2019. Crit. Rev. Oncol.-Hematol. 143, 148–152.
Huang, H., Li, T., Jiang, M., Wei, C., Ma, S., Chen, D., Tong, W., Huang, X., 2020a. Biosens. Bioelectron. 152, 112001.
Huang, M., Yang, J., Wang, T., Song, J., Xia, J., Wu, L., Wang, W., Wu, Q., Zhu, Z., Song, Y., 2020b. Angew. Chem. Int. Ed. 59, 4830–4835.
Huang, X., Hu, X., Song, S., Mao, D., Lee, J., Koh, K., Zhu, Z., Chen, H., 2020c. Sensor. Actuator. B Chem. 305, 127543.
Jiang, Y., Shi, M., Liu, Y., Wan, S., Cui, C., Zhang, L., Tan, W., 2017. Angew. Chem. Int. Ed. 56 (39), 11916–11920.
Jiang, Z., Guan, J., Qian, J., Zhan, C., 2019. Biomater. Sci. 7, 461–471.
Jung, H., Park, S., Gunassekaran, G.R., Jeon, M., Cho, Y.-E., Baek, M.-C., Park, J.Y., Shim, G., Oh, Y.-K., Kim, I.-S., Kim, C., Lee, B., 2019. Canc. Res. 79 (16), 4271–4280.
Lai, W.Y., Huang, B.T., Wang, J.W., Lin, P.Y., Yang, P.C., 2016. Mol. Ther. Nucleic Acids 5 (12), e397.
Lim, J.K., Yeap, S.P., Che, H.X., Low, S.C., 2013. Nanoscale Res. Let. 8 (1), 1–14.
Liu, L., Klausen, L.H., Dong, M., 2018. Nano Today 23, 40–58.
Lu, L., Qi, H., Zhu, J., Sun, W.X., Zhang, B., Tang, C.Y., Cheng, Q., 2017. Biomed. Pharmacother. 92, 187–195.
Lyu, H., Li, M., Jiang, Z., Liu, Z., Wang, X., 2019. Comput. Struct. Biotechnol. J. 2019 (17), 1020–1030.
Ma, J., Wu, J., Zheng, J., Liu, L., Zhang, D., Xu, X., Yang, X., Tong, Z., 2012. Microporous Mesoporous Mater. 151, 325–329.
Mei, Q., Ding, X., Chen, Y., Hong, J., Koh, K., Lee, J., Chen, H., Yin, Y., 2012. Microchim. Acta 178, 301–307.
Pang, Y., Shi, J., Yang, X., Wang, C., Sun, Z., Rui, X., 2020. Biosens. Bioelectron. 148, 11180.
Qi, G.-B., Gao, Y.-J., Wang, L., Wang, H., 2018. Adv. Mater. 30 (22), 1703444.
Takeuchi, M., Doi, T., Obayashi, K., Hirai, A., Iwai, Y., 2018. Immunol. Lett. 196, 155–160.
Tang, H., Chen, J., Nie, L., Kuang, Y., Yao, S., 2007. Biosens. Bioelectron. 22 (6), 1061–1067.
Thielbeer, F., Donaldson, K., Bradley, M., 2011. Bioconjugate Chem. 22 (2), 144–150.
Wang, L., Wang, H., Chen, H., Wang, W., Chen, X., Geng, Q., Xia, Z., Lu, Y., 2015. Oncotarget 6 (38), 41228.
Wang, H., Han, Y., Li, C., Shi, H., Lan, J., Li, Z., Zhang, Y., Liang, L., Fang, J.-Y., Xu, J., 2019a. Nat. Chem. Biol. 15, 42–50.
Wang, J., Sun, J., Liu, L.N., Flies, D.B., Nie, X., Toki, M., Zhang, J., Song, C., Zarr, M., Zhou, X., Han, X., Archer, K.A., Neill, T.O., Herbst, R.S., Boto, A.N., Sanmamed, M.F., Langermann, S., Rimm, D.L., Chen, L., 2019b. Nat. Med. 25, 656–666.
Wei, G., Wang, Y., Huang, X., Hou, H., Zhou, S., 2018. Small Methods 2 (9), 1700358.
Wei, L., Wang, X., Li, C., Li, X., Yin, Y., Li, G., 2015. Biosens. Bioelectron. 71, 348–352.
Wu, L., Ding, H.M., Qu, X., Shi, X., Yang, C., 2020. J. Am. Chem. Soc. 142, 4800–4806.
Xiong, N., Zhao, Y., Dong, X., Zheng, J., Sun, Y., 2017. Small 13 (13), 1601666.
Xu, H., Yang, Y., Wu, Q., Zhang, Y., 2020. Iran. J. Immunol. 17 (1), 1–13.
Xue, T., Wang, W.G., Zhou, X.Y., Li, X.Q., 2018. Pathology 50, 725–729.
Yang, J., Hu, L., 2019. Med. Res. Rev. 39, 265–301.
Zhai, C., Schreiber, C., Padilla-Coley, S., Oliver, A.G., Smith, B.D., 2020. Angew. Chem. Int. Ed. 59 (52), 23740–23747.
Zhao, J., Liang, D., Gao, S., Hu, X., Koh, K., Chen, H., 2019. Biosens. Bioelectron. 141, 111440.
Zhou, J., Yu, G., Huang, F., 2017. Chem. Soc. Rev. 46, 7021–7053.
Zhu, X., Lang, J., 2017. Oncotarget 8 (57), 97671–97682.
Zhu, Z., Li, H., Xiang, Y., Koh, K., Chen, H., 2020. Microchim. Acta 187 (6), 327.
Zou, L., Hong, W., He, B., Zeng, L., Tao, T., Cao, H., He, X., Zhang, Z., Guo, S., Li, Y., 2016. Theranostics 6 (6), 762–772.